SIMULATIONS OF 3-D DOMAIN WALL STRUCTURES IN THIN FILMS

XIAO-PING WANG AND KE WANG
Department of Mathematics
Hong Kong University of Science and Technology
Clear Water Bay, Kowloon, Hong Kong

WEINAN E
Department of Mathematics
Princeton University
Princeton, N.J. 08544, USA

ABSTRACT. Using the Gauss-Seidel projection method developed in [4] and [17], we simulate the three dimensional domain wall structures for thin films at various thickness. We observe transition from Néel wall to cross-tie wall and to Bloch wall as the thickness is increased. Periodic structures for cross-tie wall are also studied. The results are in good agreement with the experimental observations. Hysteresis loops are calculated for samples of various sizes. In particular, we study the effect of cross-tie wall in the switching process. These simulations have demonstrated high efficiency of the Gauss-Seidel projection method.

1. **Introduction.** Numerical simulation based on Landau-Lifshitz-Gilbert model has become an important tool in the study of both static and dynamic issues in ferromagnetic materials [1, 2, 5, 7, 10, 12, 13, 14, 18]. In the simulation of the magnetization reversal process, it is important to be able to resolve the different small length scales involved, in particular, magnetic domain walls, and magnetic vortices, since they play important roles in the switching process [16, 15]. Such a simulation demands high accuracy and efficiency of the method being used. It is well known that the most expensive part of the simulation is the calculation of demagnetization field (or stray field). The Fast Fourier Transform can be easily used to speed up the calculation [19] when the sample shape is of rectangular shape. Another difficulty in the simulation is the severe time step constraint introduced by the exchange field when standard explicit integrators (like Runge-Kutta scheme) are used. The time integration can be speeded up by using implicit scheme in time (with much larger time step). However, direct implicit integrators require solving complicated, coupled systems. In [4] and [17], we introduce an implicit method whose complexity is comparable to solving the scalar heat equation implicitly. This method is based on a combination of a Gauss-Seidel implementation of a fractional-step implicit solver for the gyromagnetic term, and the projection method for the heat flow of harmonic maps. The method is shown to significantly speed up the

simulation and allows us to carry out fully resolved calculations for the switching of the magnetization in micron-sized elements in a two dimensional setting [17].

The transition from Néel wall to cross-tie walls for ferromagnetic thin films has been observed experimentally [9]. Because of the complicated three dimensional wall structure, the problem still form a challenge to theoretical analysis, although significant progresses are made in [20] [21]. First numerical results [12], as well as some later calculations [8], confirm the experimentally observed picture. But the calculations are so far limited to patterns with a small period, and also the achievable discretization is probably insufficient for the fine structure analysis.

With tremendous improvement in efficiency by the Gauss-Seidel projection method, we are now able to carried out full three dimensional simulations of ferromagnetic thin film with large sample size and with increasing thickness as well as bulk materials. We observe transition from Néel wall to cross-tie wall and to Bloch wall as the thickness of the film is increased, a phenomenon observed in the experiments. We also study how the periodic structure of the cross-tie walls depends on the dimensions of the sample. Hysteresis loops are also calculated with fine resolution of external fields.

The paper is organized as follows. In section 1, we described the Landau-Lifshitz-Gilbert model that we used. The Gauss-Seidel projection method is described in section 2. We then present the numerical results in Section 3.

2. **The Landau-Lifshitz-Gilbert model.** The relaxation process of the magnetization distribution in a ferromagnetic material is described by the Landau-Lifshitz Equation [3, 11],

$$\mathbf{M}_t = -\gamma \mathbf{M} \times \mathbf{H} - \frac{\gamma\alpha}{M_s}\mathbf{M} \times (\mathbf{M} \times \mathbf{H}) \tag{2.1}$$

where $|\mathbf{M}| = M_s$ is the saturation magnetization, and is usually set to be a constant far from the Curie temperature. The first term on the right hand side is the gyromagnetic term, with γ being the gyromagnetic ratio. The second term in the right hand side is the damping term, with α being the dimensionless damping coefficient. $\mathbf{H}$ is the local field, computed from the Landau-Lifshitz free energy functional:

$$\mathbf{H} = -\frac{\delta F}{\delta \mathbf{M}} \tag{2.2}$$

$$F[\mathbf{M}] = \frac{1}{2}\int_\Omega \left\{ \Phi\left(\frac{\mathbf{M}}{M_s}\right) + \frac{A}{M_s^2}|\nabla\mathbf{M}|^2 - 2\mu_0\mathbf{H}_e \cdot \mathbf{M} \right\} dx + \frac{\mu_0}{2}\int_{\mathbb{R}^3} |\nabla U|^2\, dx \tag{2.3}$$

In (2.3), A is the exchange constant, $\frac{A}{M_s^2}|\nabla M|^2$ is the exchange interaction energy between the spins, $\Phi(\frac{\mathbf{M}}{M_s})$ is the energy due to material anisotropy, μ_0 is the permeability of vacuum ($\mu_0 = 4\pi \times 10^{-7} N/A^2$ in the S.I.), $-2\mu_0\mathbf{H}_e \cdot \mathbf{M}$ is the energy due to the external applied field, Ω is the volume occupied by the material, and finally the last term in (2.3) is the energy due to the field induced by the magnetization distribution inside the material. This induced field $\mathbf{H}_s = -\nabla U$ can be computed by solving:

$$\Delta U = \begin{cases} \nabla \cdot \mathbf{M} & \text{in } \Omega \\ 0 & \text{outside } \Omega \end{cases} \tag{2.4}$$

together with the jump conditions

$$[U]_{\partial\Omega} = 0$$
$$\left[\frac{\partial U}{\partial \nu}\right]_{\partial\Omega} = -\mathbf{M} \cdot \nu \tag{2.5}$$

at the boundary of the domain Ω. In (2.5) we denote by $[v]_{\partial\Omega}$ the jump of v at boundary of Ω:

$$[v]_{|\partial\Omega}(x) = \lim_{\substack{y\to x \\ y\in\bar{\Omega}^c}} v(y) - \lim_{\substack{y\to x \\ y\in\Omega}} v(y)$$

The solution to equation (2.4), with boundary conditions (2.5) is:

$$\nabla U(x) = \nabla \int_\Omega \nabla N(x-y) \cdot \mathbf{M}(y)\, dy \tag{2.6}$$

where $N(x) = -\frac{1}{4\pi}\frac{1}{|x|}$ is the Newtonian potential.

The gyromagnetic term in the Landau-Lifshitz equation (2.1) is a conservative term, whereas the damping term is dissipative.

3. **The Gauss-Seidel projection method.** The full Landau-Lifshitz equation (3.7) can be rewritten in dimensionless form. Let $\mathbf{H} = M_s\mathbf{h}$, $\mathbf{H}_s = M_s\mathbf{h}_s$, $\mathbf{H}_e = M_s\mathbf{h}_e$, $\mathbf{M} = M_s\mathbf{m}$, $t \to (\mu_0\gamma M_s)^{-1}t$ and $x \to Lx$, we can write (3.7) as,

$$\mathbf{m}_t = -\mathbf{m}\times\mathbf{h} - \alpha\,\mathbf{m}\times(\mathbf{m}\times\mathbf{h}) \tag{3.7}$$

where

$$\mathbf{h} = -Q(m_2\mathbf{e}_2 + m_3\mathbf{e}_3) + \epsilon\Delta\mathbf{m} + \mathbf{h}_s + \mathbf{h}_e$$

Here we have defined the dimensionless parameters $Q = \frac{K_\mu}{\mu_0 M_s^2}$, and $\epsilon = \frac{A}{\mu_0 M_s^2 L^2}$.

For our splitting procedure, we define the vector field:

$$\mathbf{f} = -Q(m_2\mathbf{e}_2 + m_3\mathbf{e}_3) + \mathbf{h}_s + \mathbf{h}_e$$

We solve equation

$$\mathbf{m}_t = -\mathbf{m}\times(\epsilon\Delta\mathbf{m}+\mathbf{f}) - \alpha\,\mathbf{m}\times\mathbf{m}\times(\epsilon\Delta\mathbf{m}+\mathbf{f})$$

in three steps (see [4] [17] for details):

Step 1: Implicit Gauss-Seidel

$$g_i^n = (1-\epsilon\Delta t\Delta_h)^{-1}(m_i^n + \Delta t f_i^n),$$

$$g_i^* = (1-\epsilon\Delta t\Delta_h)^{-1}(m_i^* + \Delta t f_i^n),, \qquad i = 1,2,3;$$

$$\begin{pmatrix} m_1^* \\ m_2^* \\ m_3^* \end{pmatrix} = \begin{pmatrix} m_1^n + (g_2^n m_3^n - g_3^n m_2^n) \\ m_2^n + (g_3^n m_1^* - g_1^* m_3^n) \\ m_3^n + (g_1^* m_2^* - g_2^* m_1^*) \end{pmatrix} \tag{3.8}$$

Step 2: Heat flow without constraints.

$$\mathbf{f}^* = -Q(m_2^*\mathbf{e}_2 + m_3^*\mathbf{e}_3) + \mathbf{h}_s^n + \mathbf{h}_e$$

$$\begin{pmatrix} m_1^{**} \\ m_2^{**} \\ m_3^{**} \end{pmatrix} = \begin{pmatrix} m_1^* - \alpha\Delta t(\epsilon\Delta m_1^{**} + f_1^*) \\ m_2^* - \alpha\Delta t(\epsilon\Delta m_2^{**} + f_2^*) \\ m_3^* - \alpha\Delta t(\epsilon\Delta m_3^{**} + f_3^*) \end{pmatrix} \tag{3.9}$$

Step 3: Projection onto S^2.

$$\begin{pmatrix} m_1^{n+1} \\ m_2^{n+1} \\ m_3^{n+1} \end{pmatrix} = \frac{1}{|m^{**}|}\begin{pmatrix} m_1^{**} \\ m_2^{**} \\ m_3^{**} \end{pmatrix} \tag{3.10}$$
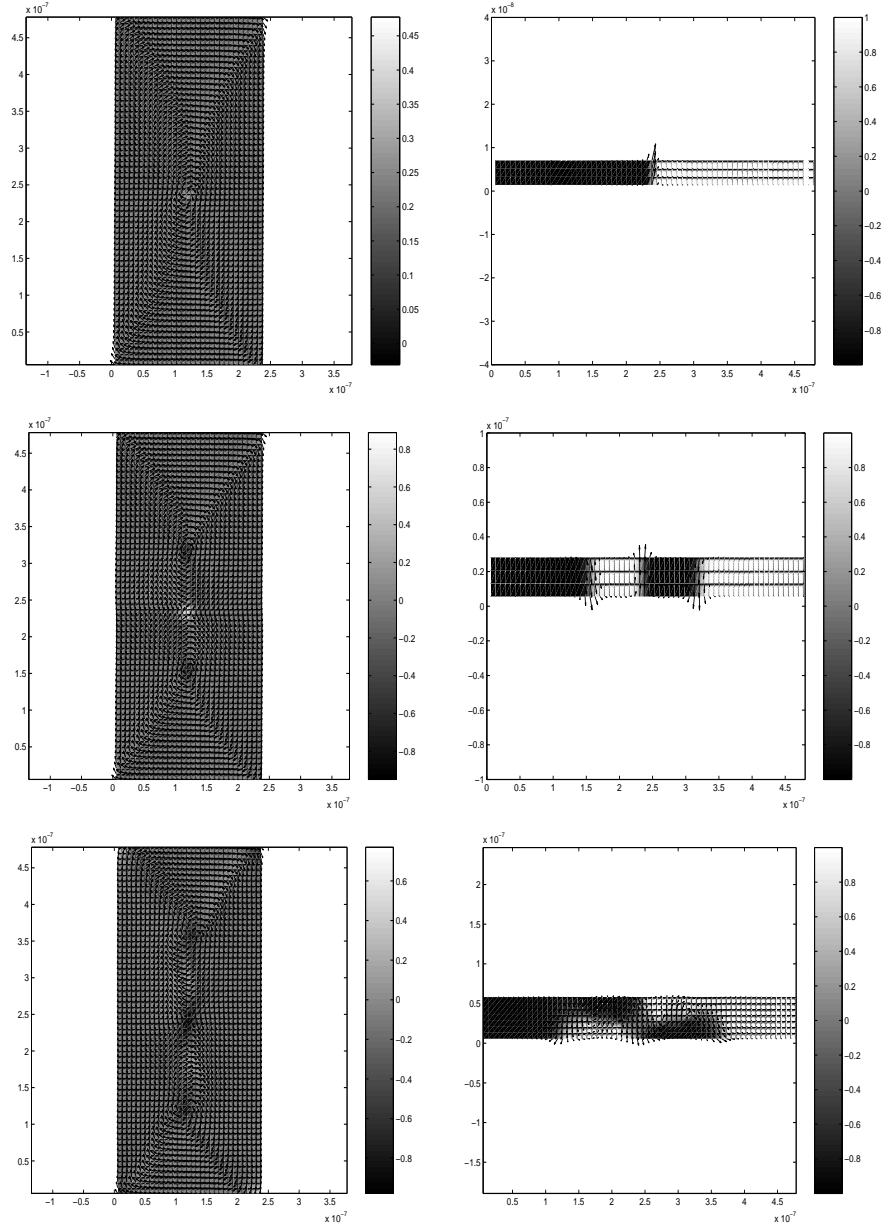
FIGURE 1. Magnetization field for xy bottom surface (left column) and yz cross sections (right column) along the center line for film of size $240nm \times 480nm$ with increasing thickness 7.5nm, 30nm and 60nm. Here and in the following figures, the in plane magnetization field components is represented by arrows and the out of plane component is represented by grey scales

4. **Computation of magnetostatic field.** In this section, we describe how to evaluate efficiently the magnetostatic field $-\nabla u$. This field is nonlocal and is formulated as a Helmholtz decomposition in the entire space. There have been two different approaches to evaluating this field. The first is to truncate the entire space to a finite size domain. The difficulty with this approach is the lack of an effective boundary condition for U. The second class of method is based on using (2.6) to compute the stray field [18][2][19].

From (2.6), we have

$$\mathbf{H}_s = \frac{1}{4\pi}\nabla\left\{\int_V \frac{\nabla\cdot\mathbf{m}(\mathbf{r}')}{|\mathbf{r}-\mathbf{r}'|}d\mathbf{r}' - \int_{\partial V}\frac{\mathbf{m}(\mathbf{r}')\cdot\mathbf{n}}{|\mathbf{r}-\mathbf{r}'|}dS(\mathbf{r}')\right\}. \tag{4.11}$$

where $\mathbf{n}$ is the outward normal direction of the material surface.

Now we consider ferromagnatic cuboid. By dividing the material V into cells V_{ijk} such that

$$V_{ijk} = [x_{i-1/2}, x_{i+1/2}] \times [y_{j-1/2}, y_{j+1/2}] \times [z_{k-1/2}, z_{k+1/2}]$$

with $x_i = idx$ and $x_{i\pm1/2} = (i\pm1/2)dx$, etc, one has

$$V = \sum_{i,j,k} V_{ijk}.$$

In each cell V_{ijk}, the computation point is located at the cell center (x_i, y_j, z_k) and $\mathbf{m}$ is regarded as a constant. Therefore the integral of divergence vanishes. For one observing point $\mathbf{r}_{ijk} = \mathbf{r}(x_i, y_j, z_k)$, the stray field can be approximated by

$$\mathbf{H}_s(\mathbf{r}_{ijk}) = \frac{1}{4\pi}\sum_{p,q,r}\int_{\partial V_{pqr}}\frac{\mathbf{r}_{ijk}-\mathbf{r}'}{|\mathbf{r}_{ijk}-\mathbf{r}'|^3}\mathbf{m}(\mathbf{r}')\cdot\mathbf{n}\,dS(\mathbf{r}'). \tag{4.12}$$

Or in componentwise, one has

$$\begin{pmatrix} H_x(x_i,y_j,z_k) \\ H_y(x_i,y_j,z_k) \\ H_z(x_i,y_j,z_k) \end{pmatrix} = \sum_{p,q,r}\begin{pmatrix} K_{xx} & K_{xy} & K_{xz} \\ K_{yx} & K_{yy} & K_{yz} \\ K_{zx} & K_{zy} & K_{zz} \end{pmatrix}_{x_{i-p},y_{j-q},z_{k-r}}\begin{pmatrix} m_x(x_p,y_q,z_r) \\ m_y(x_p,y_q,z_r) \\ m_z(x_p,y_q,z_r) \end{pmatrix}, \tag{4.13}$$

Note that each element in the demagnetization tensor can be calculated analytically and only depends on $(x_{i-p}, y_{j-q}, z_{k-r})$, which enables us to implement FFT to compute the stray field.

5. **Numerical results.** The transition from Néel wall to cross-tie wall for ferromagnetic thin films was observed experimentally [9]. Because of complicated three dimensional wall structure, the problem still forms a challenge to theoretical analysis, although theoretical results concerning the structure and the internal length scale of the cross-tie wall have appeared recently [20][21]. For the same reason, numerical simulations are limited by resolutions in the three dimensional simulations. With tremendous improvement in efficiency by our Gauss-Siedel projection method, we are able to simulate this transition with increasing thickness of the film. The simulation parameters used include exchange constant $A = 2.1^{-11}$ J/m, saturation magnetization $M_s = 1.71 \times 10^6$ $ampere/m$, anisotropy constant $K_u = 4.6 \times 10^4$ J/m^3, gyromagnetic ratio $\gamma = 1.76 \times 10^{11}$ $T^{-1}s^{-1}$ and Gilbert damping constant $\alpha = 0.1$. In all our runs, the space resolution is chosen to be $\Delta x = \Delta y = \Delta z = 3.75nm$ and time step $\delta t = 2$picosecond. A typical run costs a few hours of CPU time. For example, runs in first column in Table 1 cost 1.82 cpu hours on a 2.5 GHz Linux PC.

Transition from Néel wall to cross-tie wall and asymmetric Bloch wall

We simulate the rectangular thin film of size $L_x \times L_y \times L_z = 240 \times 480 \times d$ nm^3 with increasing thickness. Fig. 1 shows the remanent magnetization fields for bottom surface and yz cross section along the center line for three different thickness $d = 7.5, 30$ and $60nm$. The initial state is an uniform Néel structure, i.e. $m = (0, 1, 0)$ for $0 < x < L_x/2$ and $m = (0, -1, 0)$ for $L_x/2 < x < L_x$. For $d = 7.5nm$, we observe an equilibrium state with flux closure structure defined by four 90° Néel walls connecting a vortex. The yz cross section indicated that the magnetization field is uniform in the thickness direction.
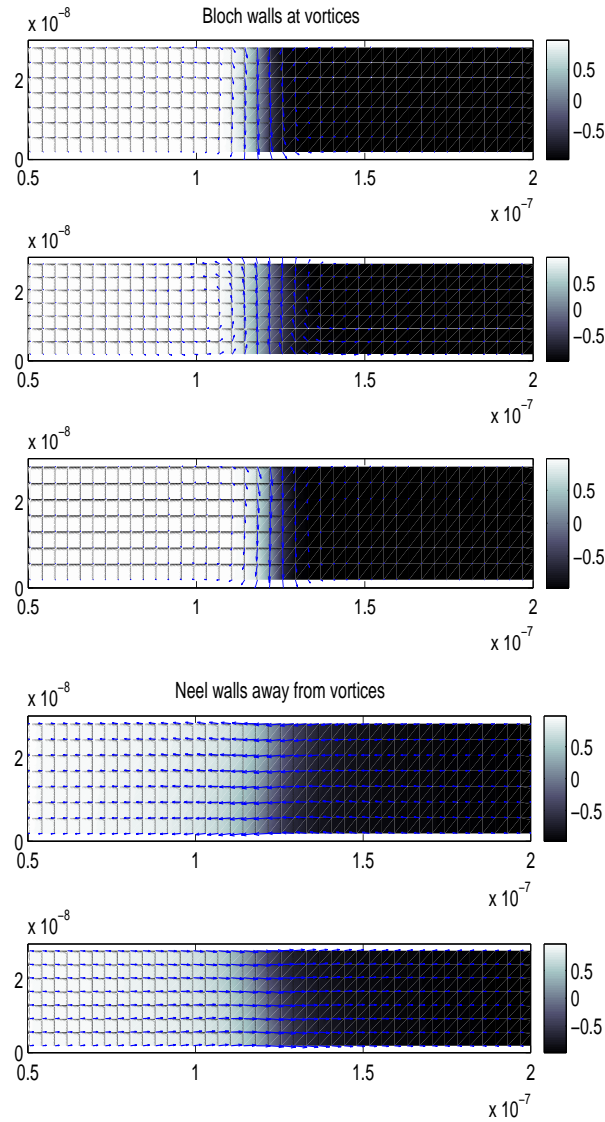
FIGURE 2. Bloch walls aross the vortices and Néel walls away from the vortices for the 30nm case.

When the thickness is increased to $d = 30nm$ and $60nm$, we observe a cross-tie state composed of four 90° Néel walls and one 180° wall with cross-tie structures consisting of two circular swirls separated by one cross swirl. Notice that for $d = 30nm$ the magnetization field is still uniform in the thickness direction and we observe symmetric Néel walls away from the vortices and the Bloch walls across the center of the vortices (see Fig. 2). In the case of thicker film of $60nm$, the magnetization field is no longer uniform in the thickness direction. Internal structure appears as shown in Fig. 1. In this case, the asymmetric Bloch wall appears in the form of vortex with 'Néel' caps on the surfaces, as shown in Fig. 3. As one moves along the wall, the vortex moves from one side to the other side with a symmetric Bloch wall in between.
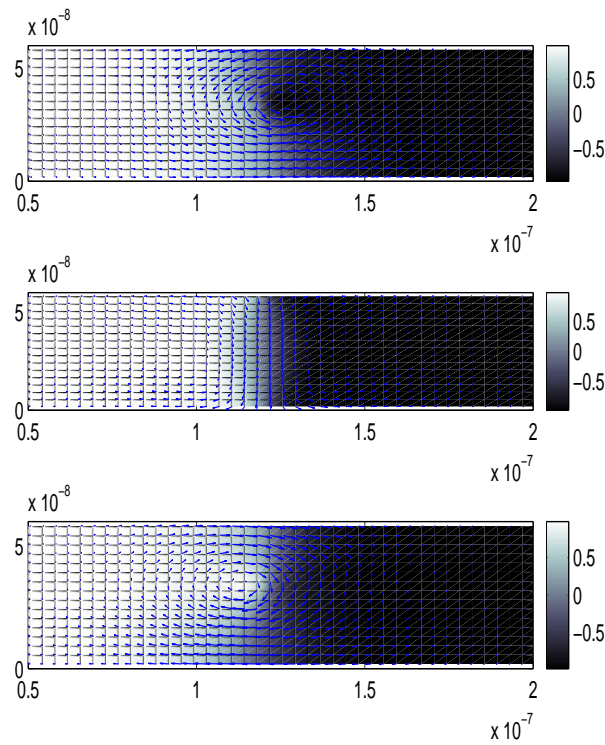

FIGURE 3.   Bloch walls aross the vortices and vortex walls away
from the vortices for the 60nm case.

When $d = 60$nm and $d = 120$nm (grid $64 \times 128 \times 16$. In Fig. 1, 4), we still observe the cross-tie wall structure at the bottom surface. But we see non-trivial structure in yz cross sections and cross-tie structure disappears as one moves up to the top surface. Internal vortices are also shown in the yz cross sections. If the thickness is further increased to $d = 240$nm, Bloch wall is clearly seen in xz cross section (Fig. 4).

Hysteresis

To study how the cross-tie wall affects the switching process, we calculate the hysteresis loop for a thin film of thickness $d = 7.5nm$ and $d = 30nm$. To simulate
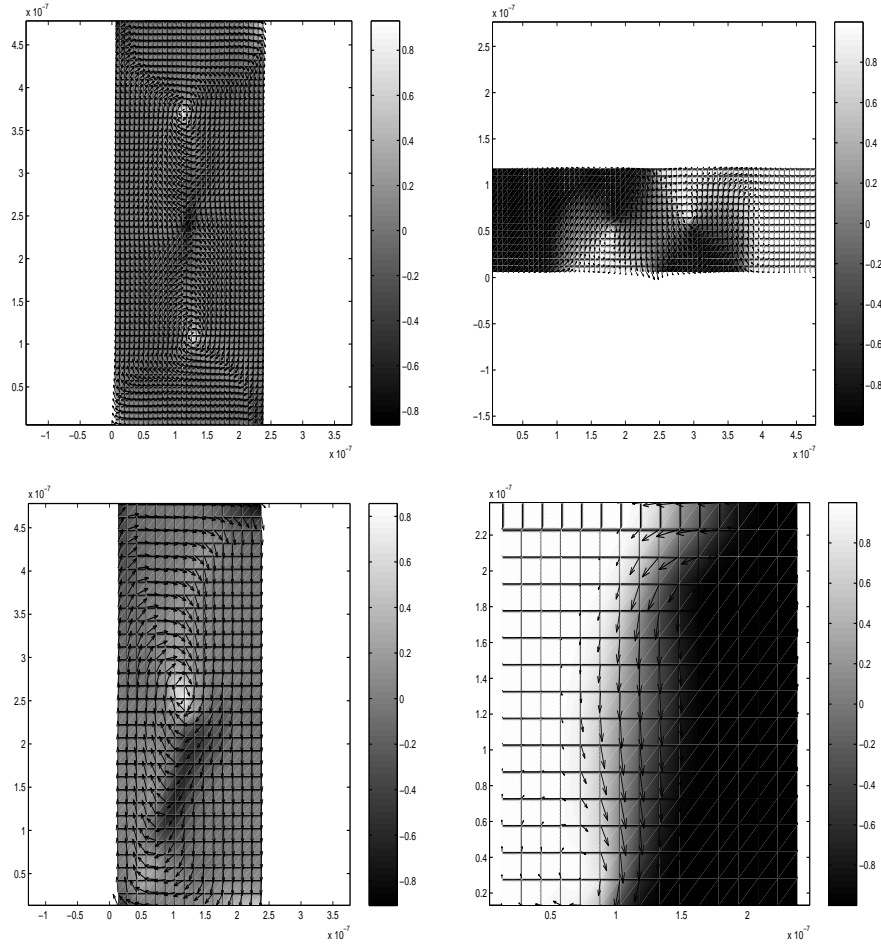
FIGURE 4. This figure shows magnetization field in bulk material. The top row is for sample of size $240nm \times 480nm \times 120nm$. Left: bottom surface; Right: yz cross section. The lower row is for sample of size $240nm \times 480nm \times 240nm$. Left: bottom surface; Right: xz cross section which displays an asymmetric Bloch wall.

the hysteresis loop, we calculate the equilibrium magnetization for each value of a varying applied field. The external field is in the x (short axis) direction. The maximum field applied are $\pm 2.5 \times 10^4 Oe$. The field increment is $10^3 Oe$. Therefore a total of 100 fields are used for the whole loop.

1. Hysteresis for a $7.5nm$ thick film sample

Figure 5 shows the hysteresis loop and intermediate vortex states corresponding to the field with red $\star$ in the loop. There seems to be a switching asymmetry. The switching field is about $-1000Oe$ at the left end of the loop when the vortices are expelled. However, it take much large field, about $1500Oe$, to drive out the vortices on the right end of the loop.

2. Hysteresis for a $30nm$ thick film sample

Fig.6 shows the hysteresis loop and intermediate vortex and cross-tie states during the first switching from right to the left and corresponding to the field with circle in the loop. The sample displays near zero remanence and coercivity when the external field is small. Hysteresis happens only for large field. It clearly shows that cross-tie wall is responsible for this type of behavior. As the positive field is decreased, a vortex is first nucleated. When the field is close to zero, cross-tie wall is formed. When the negative field is increased, the top vertex is pushed down and collide with the cross swirl and then they both disappear. The lower vortex is then pushed out of the sample as the reversal is completed.

3. Hysteresis for a cylindric sample

Figure 7, 8 show the hysteresis loop and intermediate states for a cylindric sample of size $30 \times 30 \times 120$ nm^3. A vortex is nucleated as an applied field is applied, the vortex propagates along the cylinder as the applied field is increased. Eventually the vortex is driven out of the cylinder for a strong enough field and switching is completed.

Periodic structure for the cross-tie walls

To see how the cross-tie structure depends on the size of the sample, we carried out a series of runs for samples of different sizes and with increasing thickness. The simulations show periodic structure for the cross-tie walls when the sample is large enough and the thickness is in certain range. We summarize the results in Table 1 and the magnetization fields are displayed in Fig. 9, 10 and 11. We consider samples of three different sizes starting with $120nm \times 480nm$ and then double the size in each direction. In each case, we look at how the structure changes as the thickness is increased by counting the number of cross-tie observed and measuring the width (or the period) of the cross-tie. The results in Table 1 agree with the experimental observations (Fig. 5.59 in [9]) in that the width (w) (or period) of the cross-tie wall decreases as the thickness (d) of the sample increases. The results in Table 1 also suggest that w will not change as the sample size is increased in the direction parallel to the wall (the y direction in our case). Therefore the number of the cross-tie will increase. However, if the sample is enlarged in the direction perpendicular to the wall (i.e. from $120nm$ to $240nm$ in the x direction), the width w of the cross-tie will increase. Another observation from the results in Table 1 is that the transition thickness d is also sample size (x dimension) dependent. For samples with $L_x = 120nm$, the transition from the cross-tie wall to Bloch wall starts before $d = 30$, while for samples with $L_x = 240nm$, this transition happens after $d = 30nm$.

TABLE 1. The number (n) and the width (w) of the cross-tie walls for different sample sizes (all lengths are in nanometer)

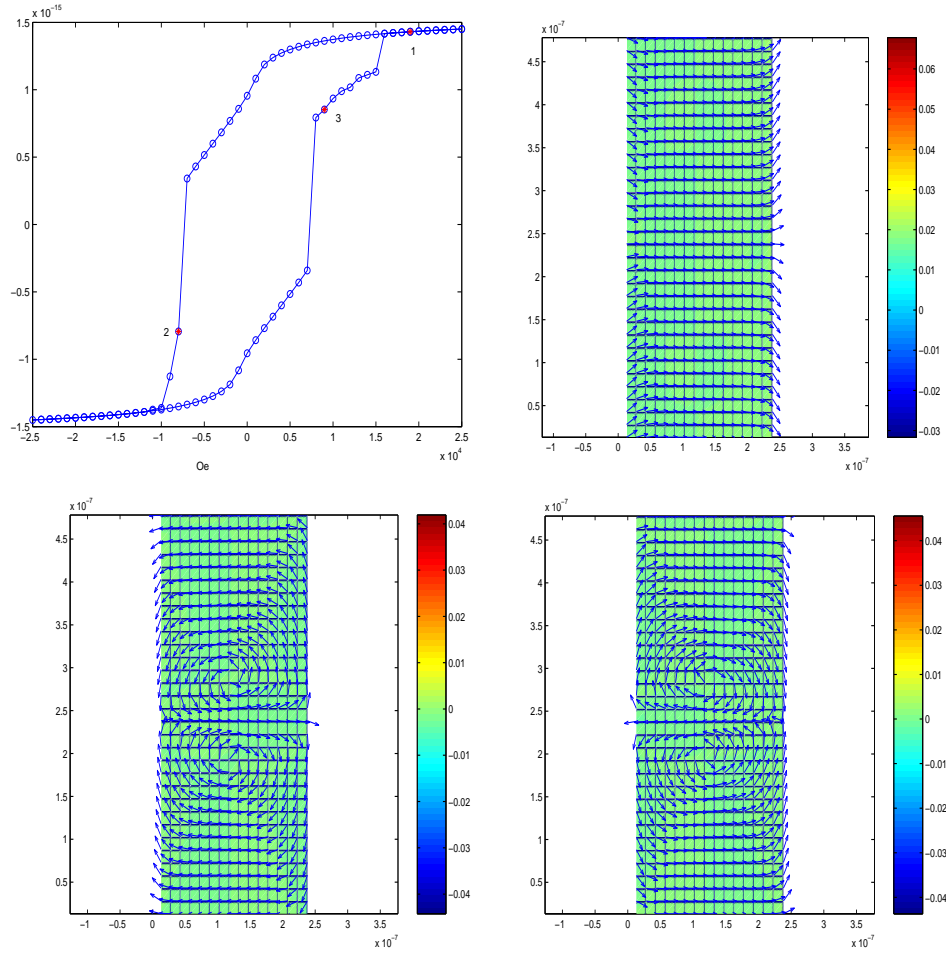|	sample size $120 \times 480 \times d$	sample size $120 \times 960 \times d$	sample size $240 \times 960 \times d$
d=15nm	n=1, w=200nm	n=4, w=200nm	n=2, w=300nm
d=20nm	n=3, w=100nm	n=8, w=100nm	n=2, w=250nm
d=30nm	transient state	transient state	n=4, w=160nm

FIGURE 5. Hysteresis loop for 7.5nm thick film of size $240nm \times 480nm$. Three intermediate states (from left to right and up and down) correspond to the red dots numbered 1-3 in the hysteresis loop.

6. **Conclusions.** In summary, we have implemented the Gauss-Siedel projection method in three dimensions for micromagnetic simulations based on Landau-Lifshitz-Gilbert system. We simulated the three dimensional domain wall structures for thin films and bulk materials. The transitions from Néel wall to cross-tie and Bloch wall are observed which agree with the experimental resutls. Periodic structures of the cross-tie walls are studied. The width of the cross-tie is shown to decrease with the thickness of the film but increase with the size in the direction perpendicular to the domain wall. The effect of cross-tie wall in the switching process is also shown in the hysteresis loop.

REFERENCES

[1] H.N. Bertram and C. Seberino, *Numerical simulations of hysteresis in longitudinal magnetic tape*, J. Magn. Magn. Mater., **193** (1999), 388–394.

[2] J.L. Blue and M.R. Scheinfein, *Using multipoles decreases computation time for magnetic self-energy*, IEEE Trans. Magn., **27** (1991), 4778–4780.

[3] W.F. Brown Jr., *Micromagnetics*, Interscience Tracts on Physics and Astronomy. Interscience Publishers (John Wiley and Sons), New York - London, 1963.

[4] Weinan E and X.P. Wang, *Numerical methods for the Landau-Lifshitz equation*, SIAM J. Numer. Anal., **38** (2000), 1647-1665.

[5] J. Fidler and T. Schrefl, *Micromagnetic modelling - the current state of the art* J. Phys. D: Appl. Phys., **33** (2000), R135–R156.

[6] B. Heinrich and J.A.C. Bland, Ultrathin Magnetic Structures I, Springer-Verlag, Berlin-New York, 1994.

[7] R. Hertel and H. Kronmüller, *Adaptive finite element techniques in three-dimensional micromagnetic modeling*, IEEE Trans. Magn., **34** (1998), 3922–3930.

[8] S. Huo, J.E. Bishop, J.W. Tucker, W.M. Rainforth and H.A. Davies, *Simulation of 3-D Micromagnetic Structures in Thin Iron Platelet*, IEEE Trans. Magn., **33** 1997), 4170–4172.

[9] Alex Hubert and Rudolf Schäfer, Magnetic Domains: The Analysis of Magnetic Microstructures. Springer-Verlag, Berlin-Heidelberg-New York, 1998.

[10] M. Jones and J.J. Miles, *An accurate and efficient 3d micromagnetic simulation of metal evaporated tape*, J. Magn. Magn. Mater., **171** (1997), 190–208.

[11] L. Landau and E. Lifshitz, *On the theory of the dispersion of magnetic permeability in ferromagnetic bodies*, Physikalische Zeitschrift der Sowjetunion, **8** (1935), 153–169.

[12] Y. Nakatani, Y. Uesake, and N. Hayashi, *Direct solution of the Landau-Lifshitz-Gilbert equation for micromagnetics*, Japanese Journal of Applied Physics, **28** (1989), no. 12, 2485–2507.

[13] Y. Nakatani, Y. Uesake, N. Hayashi, and H. Fukushima, *Computer simulation of thermal fluctuation of fine particle magnetization based on the Langevin equation*, J. Magn. Magn. Mater., **168** (1997), 347–351.

[14] W. Rave and A. Hubert, *The magnetic ground state of a thin-film element*, IEEE Trans. Magnetics, **36** (2000), 3866–3899.

[15] J. Shi, S. Tehrani, and M.R. Scheinfein, *Geometry dependence of magnetization vortices in patterned submicron NiFe elements*, Applied Physics Letters, **76** (2000), 2588–2590.

[16] J. Shi, T. Zhu, S. Tehrani, Y.F. Zheng, and J.-G. Zhu, *Magnetization vortices and anomalous switching in patterned NiFeCo submicron arrays*, Applied Physics Letters, **74** (1999), 2525–2527.

[17] X.P. Wang, Carlos J. Garcia-Cervera and Weinan E, *A Gauss-Seidel Projection Method for Micromagnetics Simulations*, J. Comp. Phys., **171** (2001), 357 - 372.

[18] Samuel W. Yuan and Neal Bertram, *Fast adaptive algorithms for micromagnetics*, IEEE Transactions on Magnetics, **28** (1992), no. 5, 2031–2036.

[19] N. Hayashi, K. Saito and Y. Nakatani, *Calculation of demagnetizing field distribution based of Fast Fourier Transform of Convolution*, Jpn J. Appl. Phys., **35** (1996), 6065–6073.

[20] A. DeSimone, R. Kohn, S. Muller and F. Otto, *Repulsive interaction of Néel walls and the internal length scale of the cross-tie wall*, Multiscale Modeling and Simulation, **1** (2003), 57-104

[21] F. Alouges, T. Rivére and S. Serfaty, Néel and cross-tie wall energies for planar micromagnetic configurations, ESAIM : COCV, 8, volume dedicated to Jacques-Louis Lions, (2002), 31-68.

E-mail address: `mawang@ust.hk`
E-mail address: `weinan@princeton.edu`
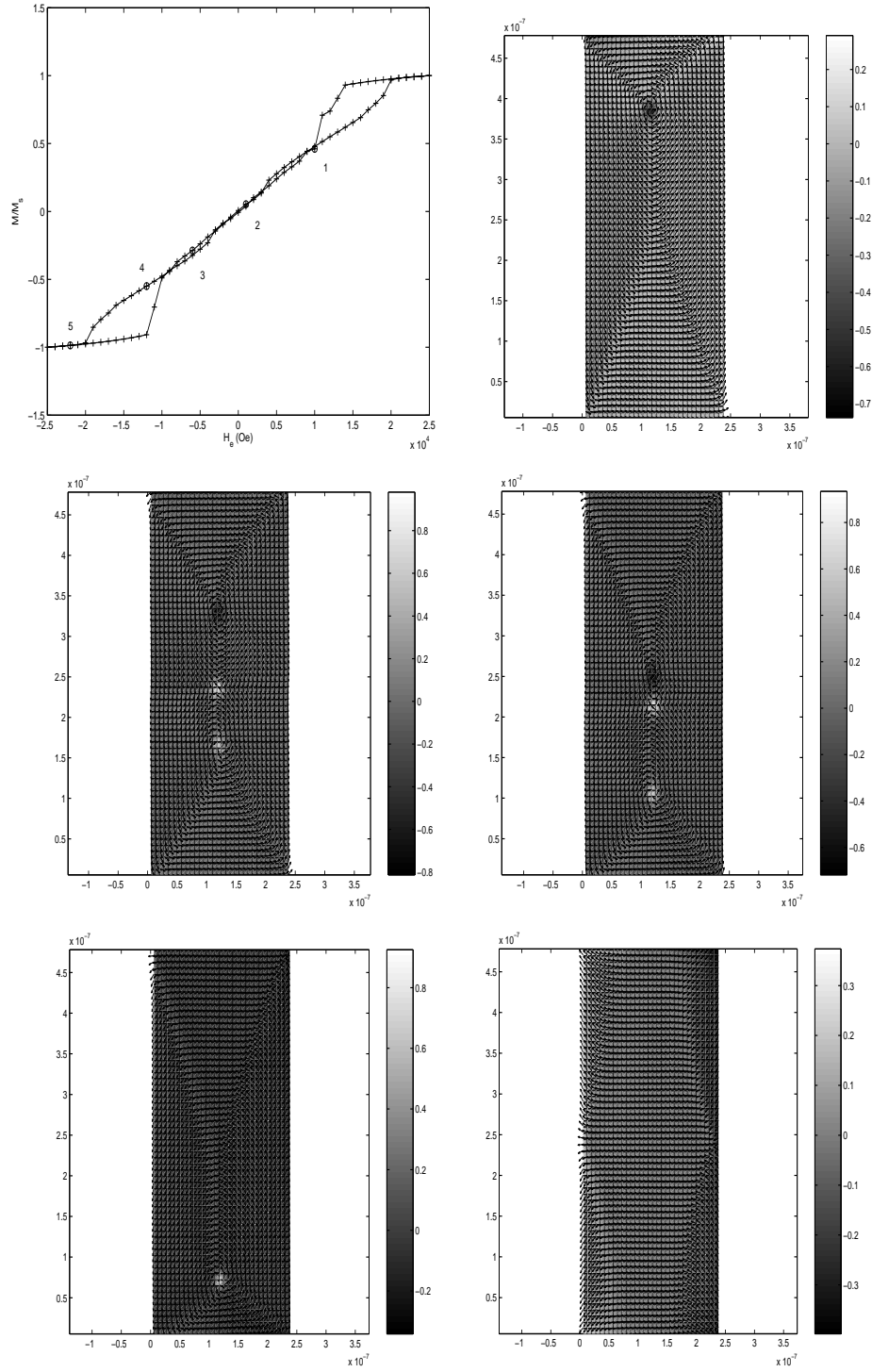
FIGURE 6. Hysteresis for 30 nm thick film of size $240nm \times 480nm$. Five intermediate states (from left to right and up and down) correspond to the circle numbered 1-5 in the hysteresis loop.
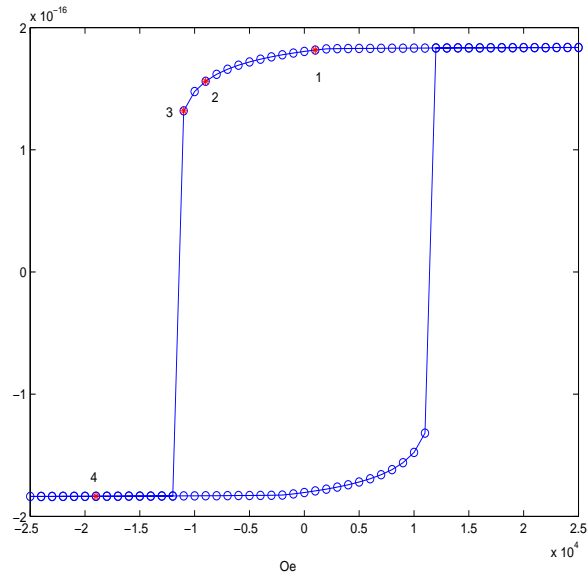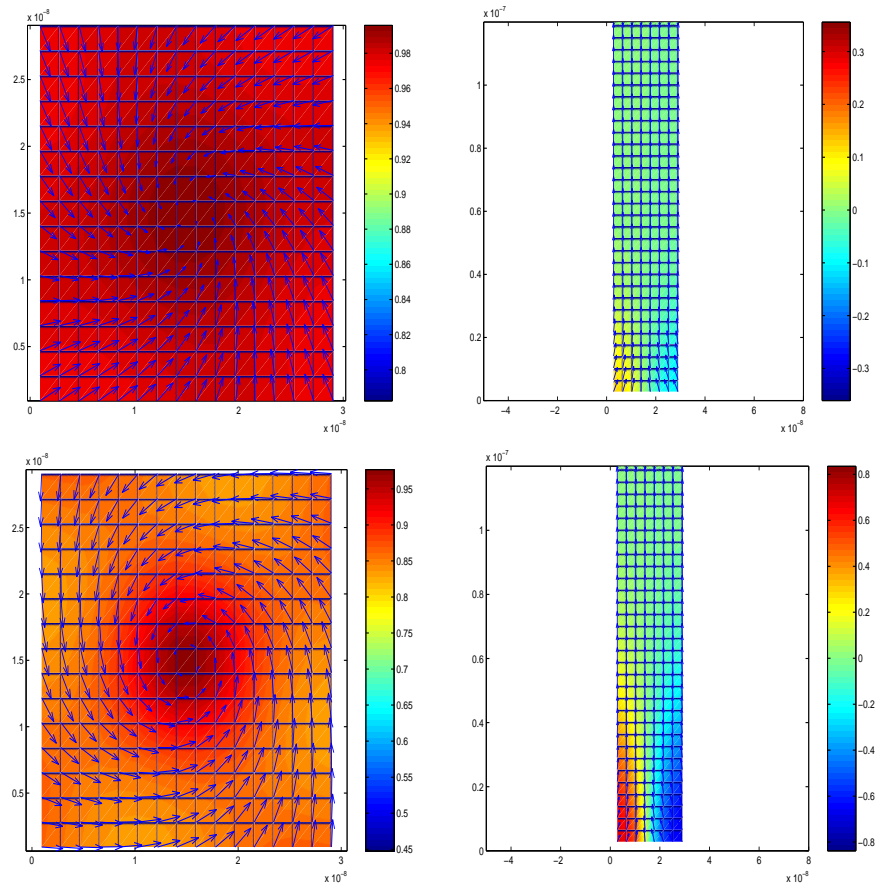
FIGURE 7.   Hysteresis loop for cylindric sample of size $30 \times 30 \times 120$ nm^3. The applied field is in the long axis direction.
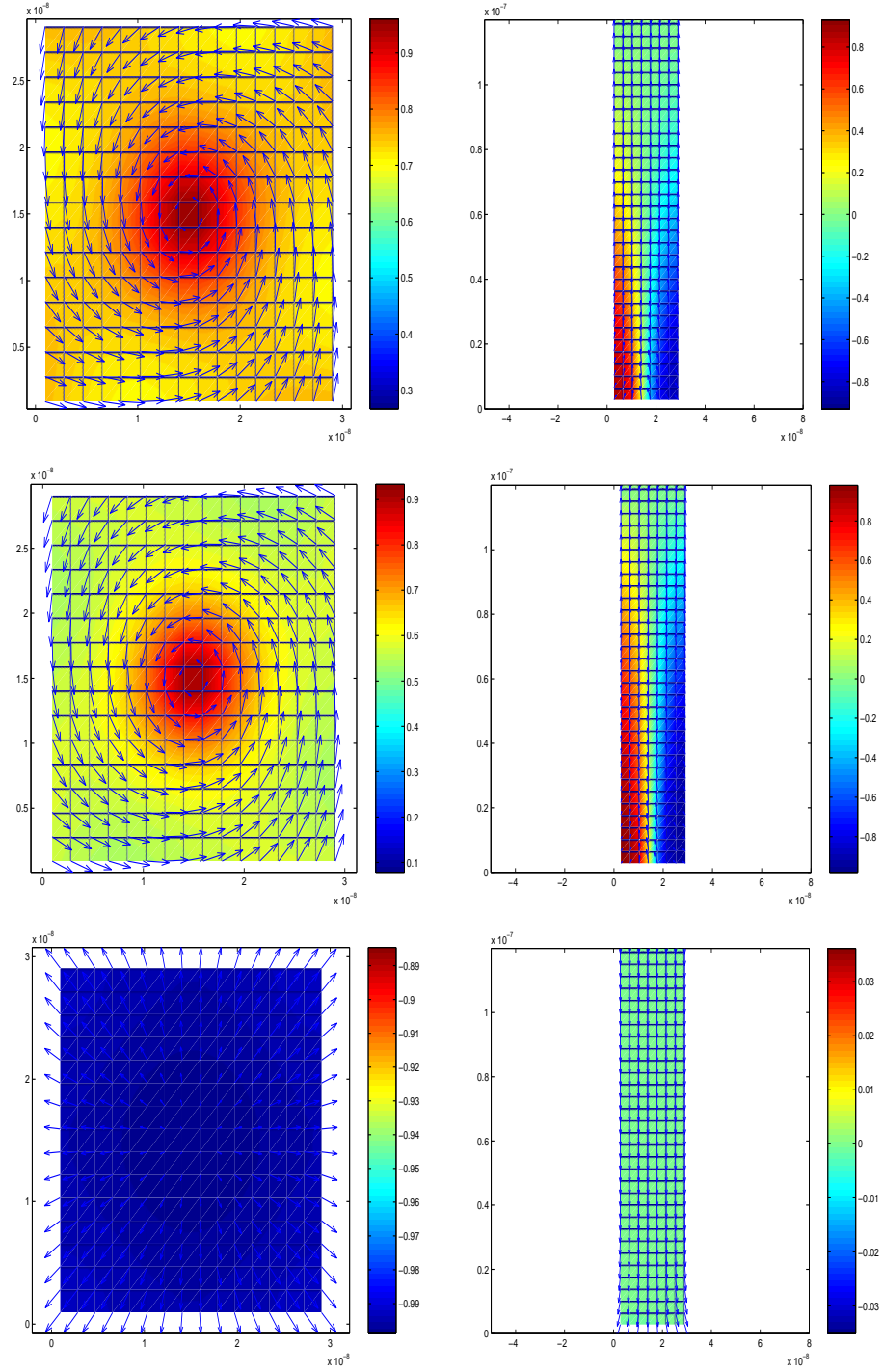
FIGURE 8.   Magnetization distributions of intermediate states correspond to the red dots numbered 1-5 in the hysteresis loop. Bottom surface (left column) and xz cross section (right column).
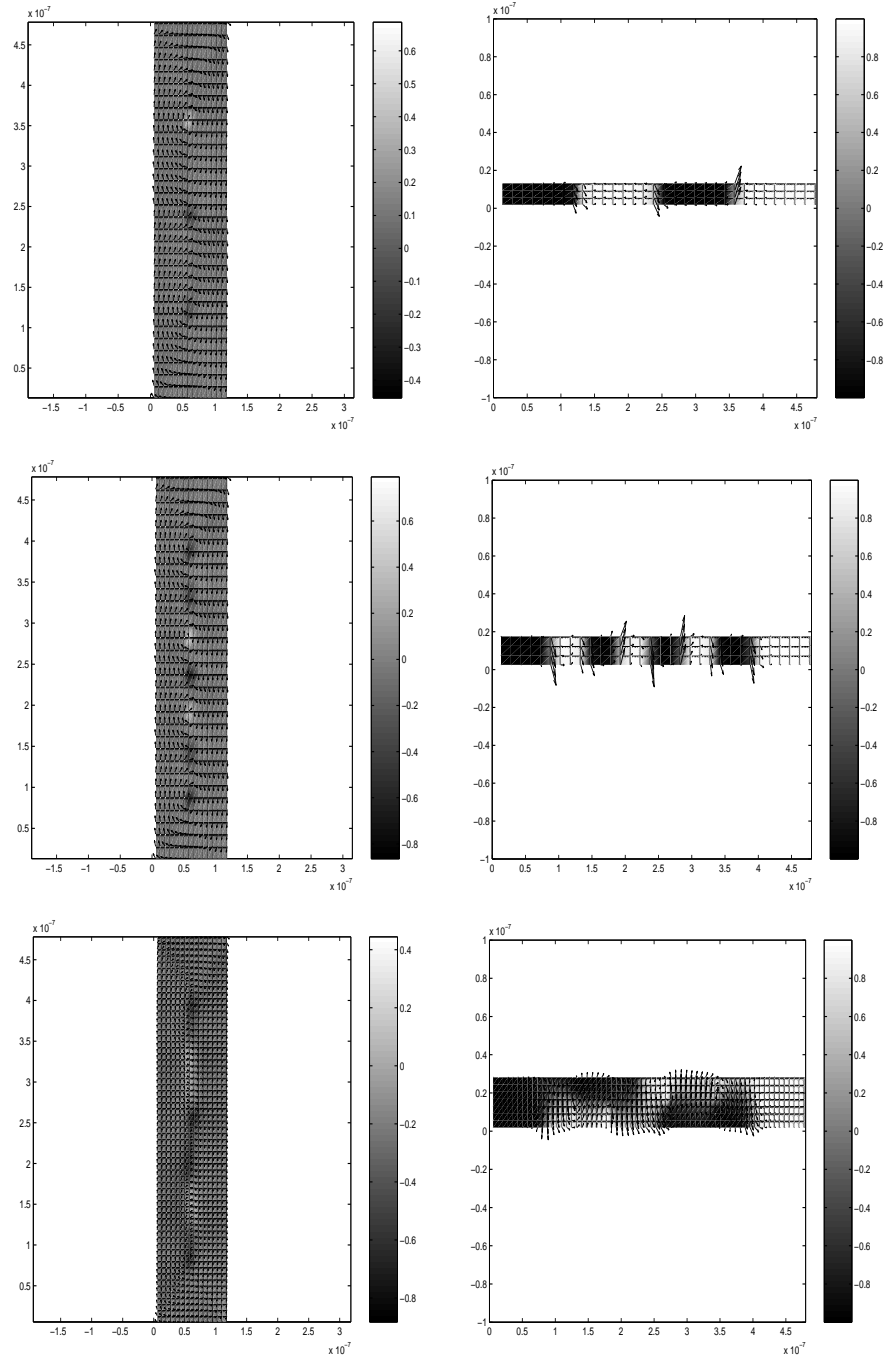
FIGURE 9.   The magnetization field for sample size $120nm \times 480nm$ and increasing thickness $d = 15, 20, 30nm$. Left: bottom surface; Right: yz cross section.
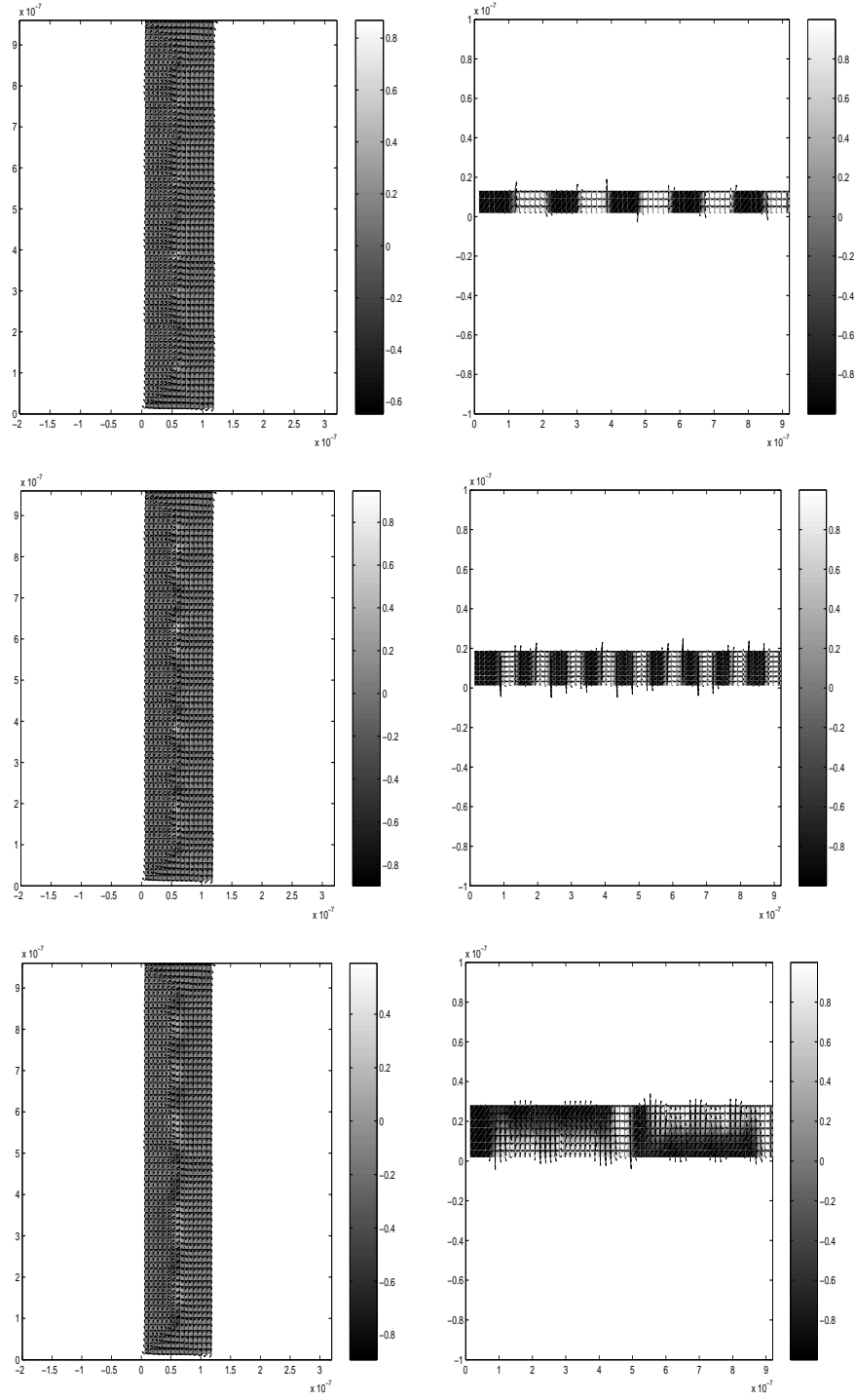
FIGURE 10. The magnetization field for sample size $120nm \times 960nm$ and increasing thickness $d = 15, 20, 30nm$. Left: bottom surface; Right: yz cross section.
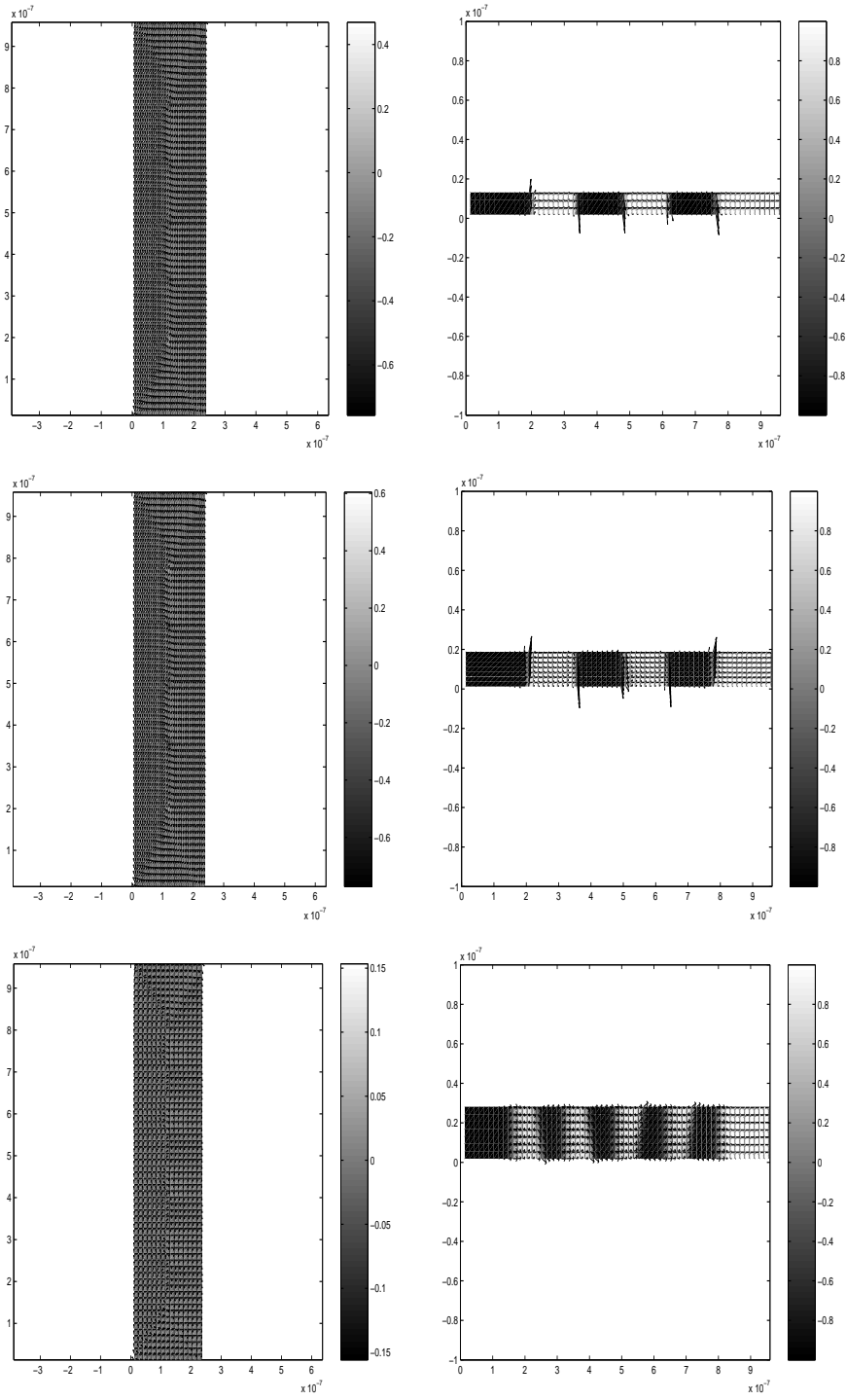
FIGURE 11. The magnetization field for sample size $240nm \times 960nm$ and increasing thickness $d = 15, 20, 30nm$. Left: bottom surface; Right: yz cross section.